buildings

MDPI

Article

Design Equations for Predicting Stability of Unlined Horseshoe Tunnels in Rock Masses

Jintara Lawongkerd [1], Jim Shiau [2], Suraparb Keawsawasvong [1,*], Sorawit Seehavong [1] and Pitthaya Jamsawang [3]

[1] Department of Civil Engineering, Thammasat School of Engineering, Thammasat University, Pathumthani 12120, Thailand
[2] School of Engineering, University of Southern Queensland, Toowoomba QLD 4350, Australia
[3] Soil Engineering Research Center, Department of Civil Engineering, King Mongkut's University of Technology North Bangkok, Bangkok 10800, Thailand
* Correspondence: ksurapar@engr.tu.ac.th

Abstract: This paper aims to propose new stability equations for the design of shallow, unlined horseshoe tunnels in rock masses. The computational framework of the upper- and lower-bound finite-element limit analysis is used to numerically derive the stability solutions of this problems using the Hoek–Brown failure criterion. Five dimensionless parameters including the width ratio and the cover-depth ratio of the tunnels, as well as the normalized uniaxial compressive strength, the geological strength index, and the yield parameters of the Hoek–Brown rock masses, are considered in the study. Selected failure mechanisms of the horseshoe tunnels in rock masses are presented to portray the effect of all dimensionless parameters. New design equations for stability analyses of horseshoe tunnels are developed using the technique of nonlinear regression analysis and the average bound solutions. The proposed stability equations are highly accurate and can be used with great confidence by practitioners.

Keywords: horseshoe tunnels; rock mass; Hoek–Brown; finite-element-limit analysis; design equation

Citation: Lawongkerd, J.; Shiau, J.; Keawsawasvong, S.; Seehavong, S.; Jamsawang, P. Design Equations for Predicting Stability of Unlined Horseshoe Tunnels in Rock Masses. *Buildings* **2022**, *12*, 1800. https://doi.org/10.3390/buildings12111800

Academic Editor: Erwin Oh

Received: 28 September 2022
Accepted: 21 October 2022
Published: 27 October 2022

1. Introduction

The uses of horseshoe-shaped sections are not uncommon in the construction of tunnels and subways, particularly in mountainous areas where rock excavation is needed. Indeed, the semi-elliptical roof of the horseshoe-shaped tunnel has advantages in distributing the loads through geometrical arches. Furthermore, the semi-circular space above the tunnel is needed for maintenance considerations. To assure safety while employing an open-face classical tunneling technique to construct the unusual horseshoe-shaped tunnel, a thorough stability analysis is thus essential.

Previous studies on the tunnel stability of soils using laboratory and centrifuge experiments were conducted by [1–3]. By using an analytical approach of the limit analysis method, Davis et al. [4] proposed analytical solutions for a cohesive-soil, shallow-tunnel problem. Sloan [5] has introduced the finite-element limit-analysis (FELA) approach to conduct the numerical solutions and has applied FELA to analyze the tunnel stability problem with different shapes such as unlined circular tunnels, unlined square and rectangular tunnels, plane strain tunnel headings, 3D headings of tunnels and sinkholes and soil retention stability with openings in subterranean walls, e.g., [6–23].

Research on horseshoe-shaped tunnels has not received much attention till the recent investigation on the undrained stability of horseshoe tunnels in undrained clays [24]. Bhattacharya and Sriharsha [25] have recently presented lower-bound solutions for the problem of drained horseshoe tunnels. The effect of spacing between the dual horseshoe tunnels in undrained clay was also investigated by [26,27]. Moreover, there were various analytical investigations on horseshoe tunnel stability, e.g., [28–32].

Regarding rock tunnel excavation, the well-recognized failure criterion to describe the rock behavior is the Hoek–Brown (HB) failure criterion [33]. While determining the shear strength of rock masses, the HB-failure criterion takes into account the nonlinearity of the minor principal (compressive) stress in contrast to the Mohr–Coulomb failure criterion, and therefore better represents the crucial failure aspects of various rock types. By using the combination of the Finite-Element-Limit Analysis (FELA) and the HB model, several previous papers have presented a number of rock-tunnel-stability solutions such as for unlined circular tunnels, unlined square and rectangular tunnels, unlined horseshoe tunnels using the lower-bound method and planar tunnel headings, e.g., [34–41].

It was noted that the problem of horseshoe-shaped tunnels in rock masses has not been extensively investigated with the efficiency tools of both the upper-bound (UB) and lower-bound (LB) methodology of an adaptive-finite-element method. In this paper, stability charts and equations are established from the upper- and lower-bound solutions to handle the stability problem of unlined rock tunnels with horseshoe shapes. However, there are no design equations that enable an evaluation of unlined rock tunnels with horseshoe shapes in the available published literature. The proposed design equations were developed using a nonlinear regression analysis and are useful in practice for geotechnical engineers to assess the stability of traditional open-face tunneling in maintaining tunnel excavation stability.

2. Hoek–Brown (HB) Failure Criterion

The Hoek–Brown failure criterion [42] is employed in this study to produce the stability solutions of unlined horseshoe tunnels. The power law relationship between the major and minor principal stresses is used to describe the formulation of the HB-failure criterion (i.e., σ_1 and σ_3). Equation (1) gives a mathematical representation of the HB model with the assumption of positive tensile normal stresses (see [42]).

$$-\sigma_3 = -\sigma_1 + \sigma_{ci}\left(-m_b\frac{\sigma_1}{\sigma_{ci}} + s\right)^a \tag{1}$$

where σ_{ci} represents the uniaxial compressive strength. The mathematical expressions for the parameters m_b, s, and a span from Equations (2)–(4) (see [42]).

$$a = \frac{1}{2} + \frac{1}{6}\left\{\exp\left(\frac{-GSI}{15}\right) - \exp\left(\frac{-20}{3}\right)\right\} \tag{2}$$

$$m_b = m_i \exp\left(\frac{GSI - 100}{28 - 14DF}\right) \tag{3}$$

$$s = \exp\left(\frac{GSI - 100}{9 - 3DF}\right) \tag{4}$$

According to the preceding equations, the geological strength index (*GSI*) generally varies in the range of 10 for an exceedingly deficient rock mass up to 100 for an undamaged or intact rock mass. The shear strength of an intact rock mass is associated with the Hoek–Brown yield parameter (m_i), which is determined by several factors such as mineral composition and particle size. The disturbance factor or *DF* parameter indicates the level of disturbance that the explosion and stress relaxation have caused to the rock mass. In general, the *DF* spans from 0 to 1, with a *DF* of 0 being the least disturbed or undisturbed in situ rock masses, whereas the highly disturbed in situ rock masses have a *DF* of 1.

3. Problem Statement

The problem description of an unlined horseshoe tunnel surrounded by rock mass is illustrated in Figure 1. The geometry of the tunnel is separated into two parts: a flat floor underneath the ceiling with dimensions B for the width and $D/2$ for the height of the vertical walls; and a semi-elliptical tunnel ceiling with a width and height of B and $D/2$, respectively. The tunnel is positioned with a cover depth of C below the ground surface.

The rock mass behavior around the tunnel is represented using the HB criterion and γ also represents the rock unit weight. The rock surface is subject to a uniform surcharge pressure σ_s while the support pressure inside the rock tunnel is disregarded.

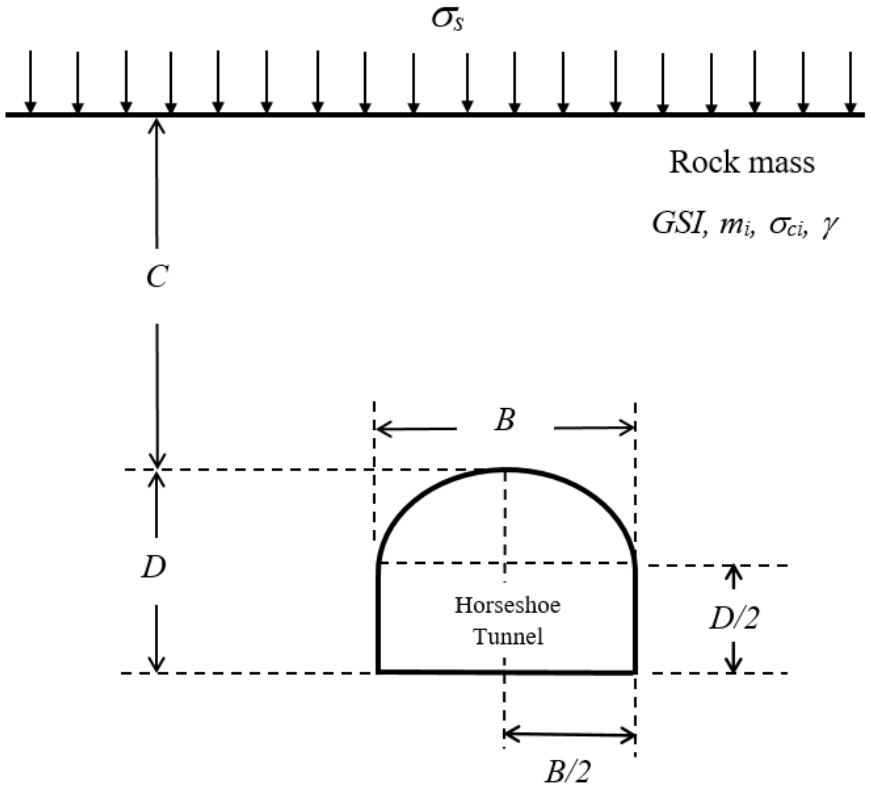

Figure 1. Problem description of a horseshoe tunnel.

Based on the present analysis, this investigation is focused on rock masses with the assumptions of $DF = 0$. In the computations in this study, the disturbance factor DF is reduced to zero due to the assumption that the tunneling excavation process causes no appreciable disturbances to the adjacent rock mass. By adopting the dimensionless technique, the six-dimensional input parameters (i.e., B, D, σ_{ci}, GSI, m_i, γ) can be reduced to four dimensionless parameters, which further result in the dimensionless output parameter (σ_s/σ_{ci}) of a uniform surcharge σ_s as indicated by Equation (5).

$$\frac{\sigma_s}{\sigma_{ci}} = f(\frac{B}{D}, \frac{C}{D}, \frac{\sigma_{ci}}{\gamma D}, m_i, GSI) \tag{5}$$

where C/D denotes the tunnel's cover-depth ratio and B/D denotes the tunnel's width ratio. $\sigma_{ci}/\gamma D$ denotes the normalized uniaxial compressive strength. σ_s/σ_{ci} denotes as the normalized collapse surcharge ratio or the stability factor that is the objective function to be "optimized" using limit analysis theorems and finite element technique. It is also named as the stability factor (σ_s/σ_{ci}) in this paper. The parametric variations considered in the present stability analysis are listed as follows.

- The tunnel cover-depth ratio of C/D = 1–5.
- The tunnel width ratio of B/D = 0.5, 0.75, 1, 1.333, and 2.
- The yield parameter m_i is set to be m_i = 5–30.
- The range of the GSI is set to be 40–100.
- The rock's unit weight is in the range from 22–30 kN/m^3 while the uniaxial compressive strength is taken in the range from σ_{ci} = 0.25–250 MPa for weak to strong rocks. As a result, the dimensionless parameter $\sigma_{ci}/\gamma D$ is set to be 100–∞, where the case of $\sigma_{ci}/\gamma D = \infty$ correlates to exceptionally high strength rock masses (σ_{ci} is quite huge).

Note that the above selected ranges were also employed by several researchers to investigate various forms of rock tunnels stability, e.g., [34–41]. There are five input data attributes related to the tunnel geometry and rock conditions that are summarized in Table 1.

Table 1. Input parameters.

Input Parameters	Values
C/D	1, 2, 3, 4, 5
B/D	0.5, 0.75, 1, 1.333, 2
GSI	40, 60, 80, 100
m_i	5, 10, 20, 30
$\sigma_{ci}/\gamma D$	100, 1000, ∞

4. Finite-Element-Limit Analysis (FELA)

The plastic bound theorems as well as finite element discretization in conjunction with the mathematical optimization are used for the presented computational limit analysis. The upper bound (UB) and lower-bound (LB) solutions can be used to bracket the rigorous collapse pressure of tunnel problems based on the associated flow rule and an assumption of a rigid plastic material. In order to enhance computational performance, this study mainly utilizes the modern adaptivity meshing approach. The active failure of horseshoe rock tunnels is calculated employing the innovative FELA software OptumG2 [43].

Three numerical models of unlined horseshoe tunnels in rock masses are shown in Figure 2a–c with B/D = 0.5, 1, 2, respectively. The plots are in the cases of C/D = 2. The simulations are performed just using a half of the domain as well as the tunnel's geometry in all numerical analyses and has no significant effect on the solution. In the FELA analysis, the standard boundary conditions are imposed with the following limitation: the movements at the left and right planes are set to occur only in the vertical direction, while the movements at the bottom plane's boundary is prohibited to occur in both vertical and horizontal directions The domain size is selected to be large enough in order to prevent the plastic shear zone intersecting the right and bottom boundaries of the domain. The sufficiently large domain can ensure that the calculated bound solutions will not be affected from an insufficient size of the domain. Inside the tunnel, there is not any pressure assigned from the central tube of the tunnel. The uniform surcharge σ_s is delivered downward to the region of the rock surface and is intended to be optimum at the active collapse event.

According to the UB formulation, the rock mass is discretized into various six-noded triangular elements with the velocity components at all the nodes. The objective function of the UB analysis is to optimize the maximum surcharge (σ_s). The kinematically admissible displacement field can be found everywhere in the domain as well as at the boundary conditions. The load is calculated from the principle of virtual work based on the compatibility and the flow rule formulations. As a result, the surcharge is related to the problem's unknown velocities by using the virtual work idea, which compares the rate of work accomplished between external loads to the internal energy dissipation at triangle components.

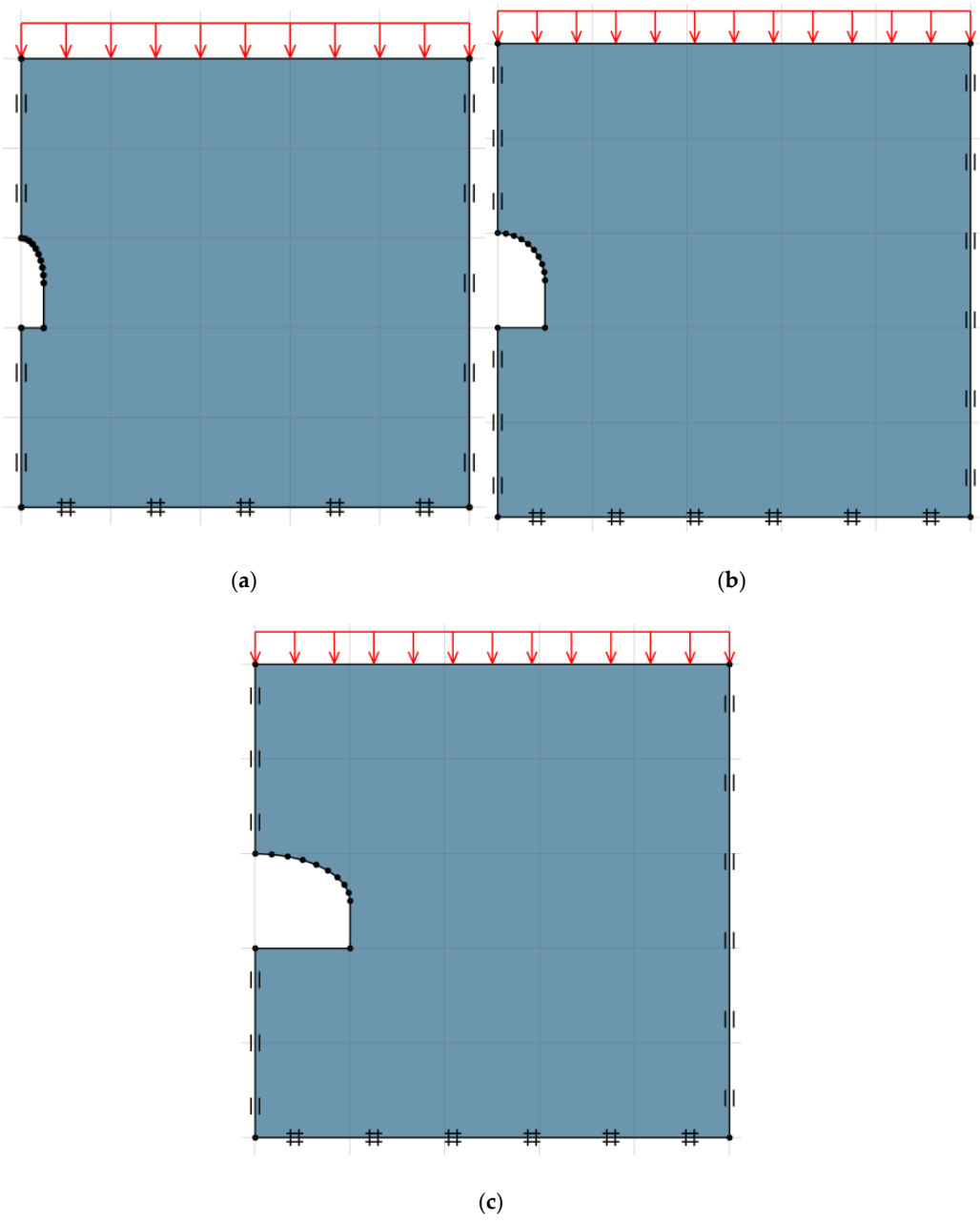

Figure 2. A numerical model of horseshoe tunnel: (**a**) B/D = 0.5, (**b**) B/D = 1 and (**c**) B/D = 2.

According to the LB formulation, the rock mass around the tunnel is partitioned by using linear interpolation inside three-nodded triangular elements, each of which nodes is connected to an unknown stress component. By allowing nodes to be specific to each element, stress discontinuities are supplied to the lower-bound mesh at the common edges of the neighboring triangular elements. The objective function in the optimization is to maximize the surcharge (σ_s) at the surface of the rock. The surcharge can be solved by taking into account the statically permissible stress constraints that employing the equilibrium equations, the stress discontinuities, and the stress boundary conditions. As a result, the problem's lower bound solution is obtained.

The powerful mesh adaptivity feature had been employed to generate the compact bound solutions [44]. It should be noted that by utilizing this feature, a variety of elements are automatically inserted in the regions that have significant plastic shear strain and where, following the given iterations, the discrepancies between the upper and lower-bound solutions become limited. This study utilized a beginning mesh of 5000 elements

with five iterations of mesh adaptivity, which leads to an expanded finalized mesh of 10,000 elements. This setting is applied to all numerical models carried out in this study by following many previous studies, e.g., [45–58]. Note that Sloan [5] stated that the stability analysis using the FELA based on the limit analysis theory requires only the conventional strength parameters such as the undrained shear strength, but does not use the deformation parameters such as Poisson's ratio and Young's modulus which are different from the conventional displacement-based FEM. Thus, Poisson's ratio and Young's modulus are not considered in this study using FELA. Hence, large deformations of rock tunnels cannot be investigated by using FELA.

5. Results and Discussion

5.1. Verification

Throughout this paper, the numerical results of all parametric studies are provided in terms of average solutions (Ave), which are the mean value from the UB and LB solutions. Note that the upper and lower-bound discrepancies are permissible up to a maximum of 5% for all numerical results presented hereafter in this paper. To verify these Ave solutions, the published LB solutions by Rahaman and Kumar [40] are applied to perform a verification with the current solutions. The instances that were picked to compare in Figure 3 include: C/D = 1–5; B/D = 1; m_i = 5; $\sigma_{ci}/\gamma D$ = 100 and ∞; GSI = 40, 60, 80, 100. It can be observed that the stability factor σ_s/σ_{ci} from the present study has a very good agreement with the previous solution. Therefore, the results that were achieved and reported in the study inspire considerable confidence. A few more parametric studies are further investigated next.

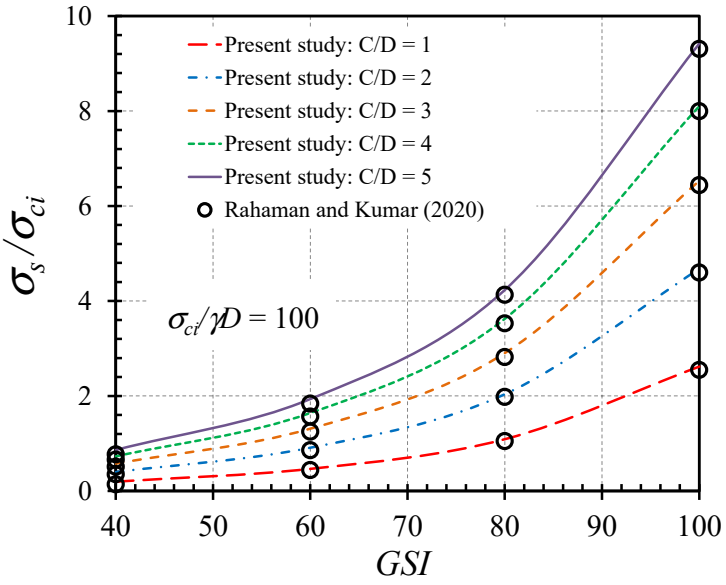

(**a**)

Figure 3. *Cont.*

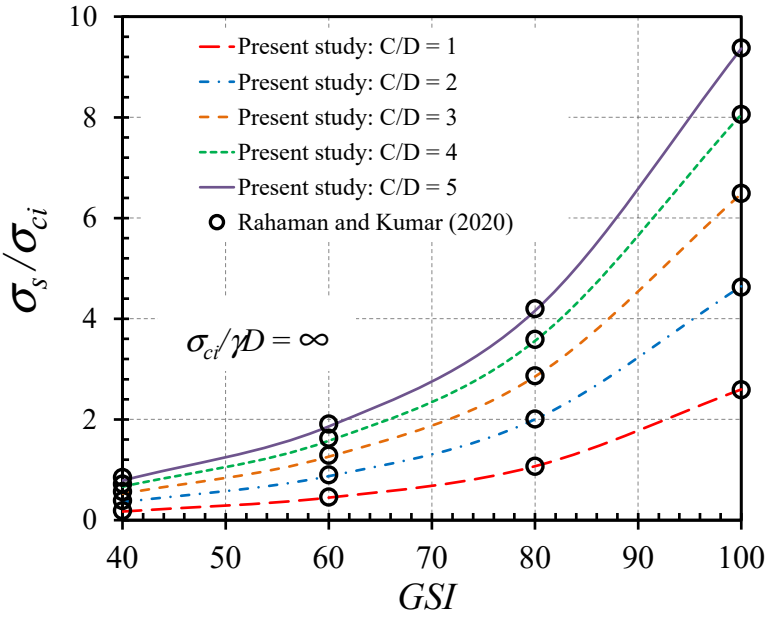

(**b**)

Figure 3. Verification of the stability factor σ_s/σ_{ci} of horseshoe tunnels with $B/D = 1$ and $m_i = 5$ between the current study to those available solutions: (**a**) $\sigma_{ci}/\gamma D = 100$ and (**b**) $\sigma_{ci}/\gamma D = \infty$.

5.2. Parametric Studies

For the stability problem of rock tunnels with a horseshoe shape, this study produces a total of 1200 computed Ave solutions of the normalized failure surcharge σ_s/σ_{ci}, which will be used later to develop design equations in the next section. In order to depict the impact of all the input parameters such as B/D, C/D, $\sigma_{ci}/\gamma D$, GSI, and m_i that are taken into consideration, the numerical results are also visually given in Figures 4–8.

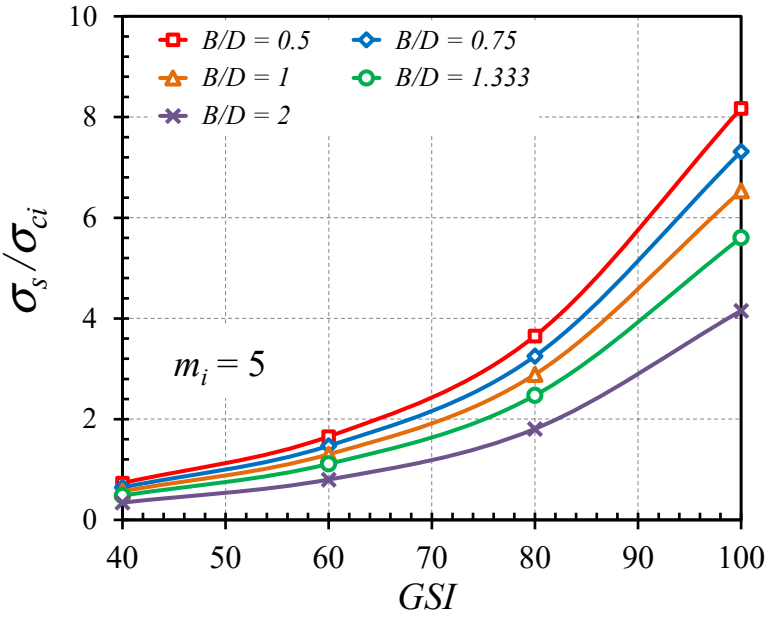

(**a**)

Figure 4. *Cont.*

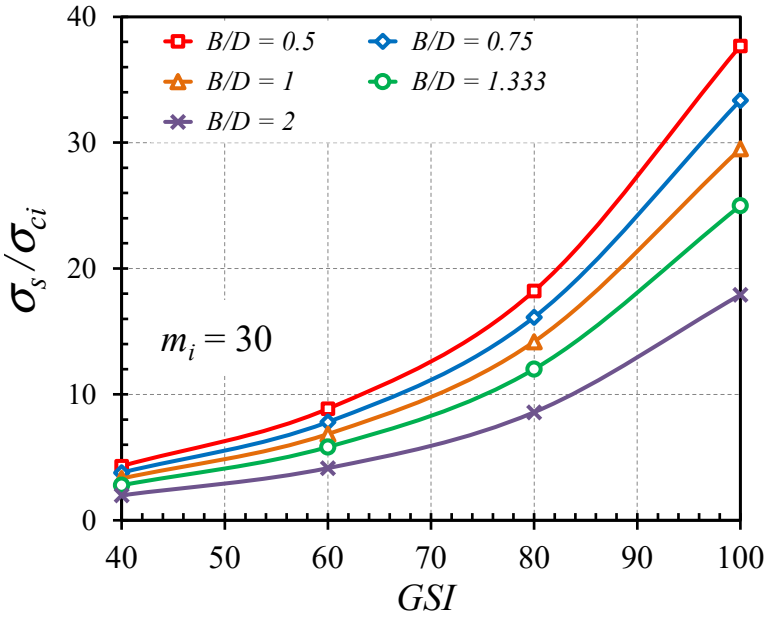

(**b**)

Figure 4. Impact of *GSI* on σ_s/σ_{ci} of horseshoe tunnels with $C/D = 3$ and $\sigma_{ci}/\gamma D = 1000$: (**a**) $m_i = 5$ and (**b**) $m_i = 30$.

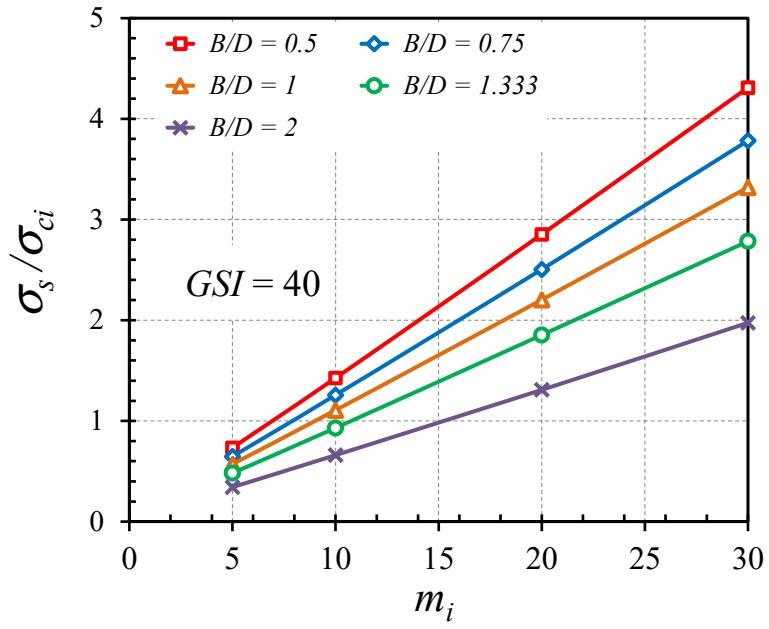

(**a**)

Figure 5. *Cont.*

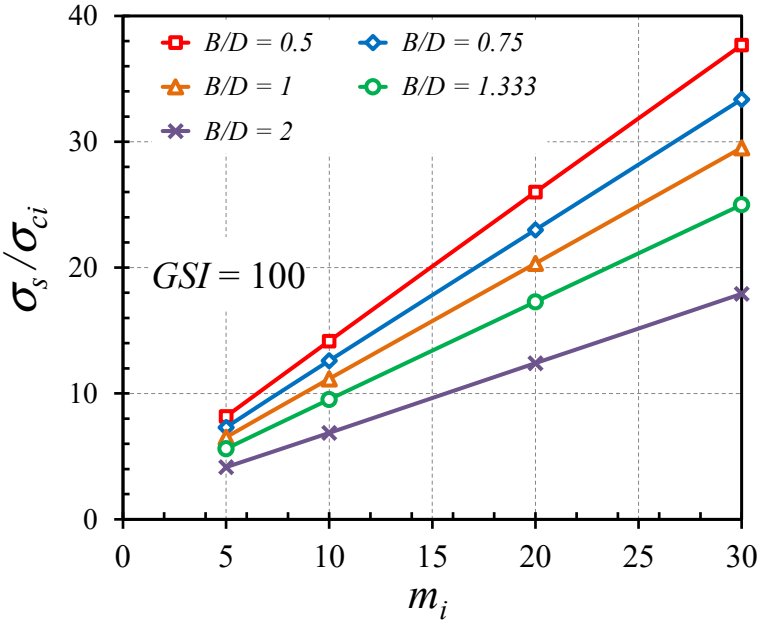

(**b**)

Figure 5. Impact of m_i on σ_s/σ_{ci} of horseshoe tunnels with $C/D = 3$ and $\sigma_{ci}/\gamma D = 1000$: (**a**) $GSI = 40$ and (**b**) $GSI = 100$.

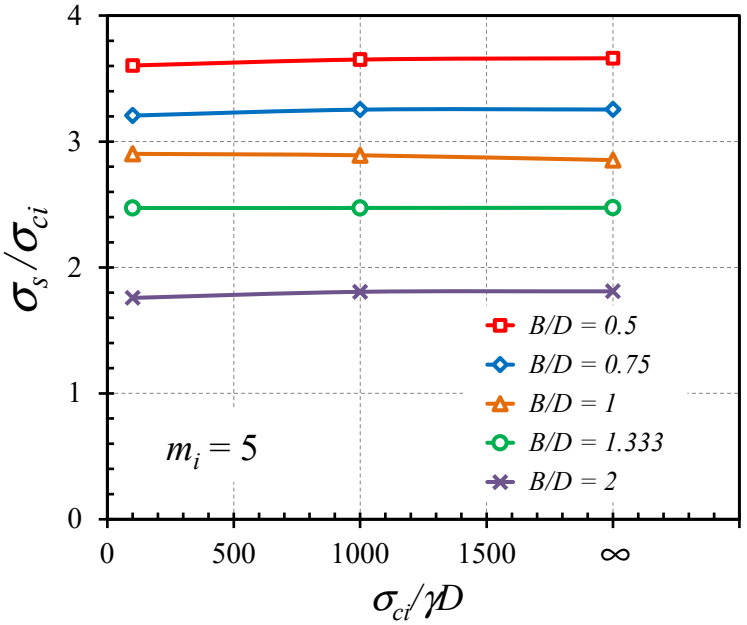

(**a**)

Figure 6. *Cont.*

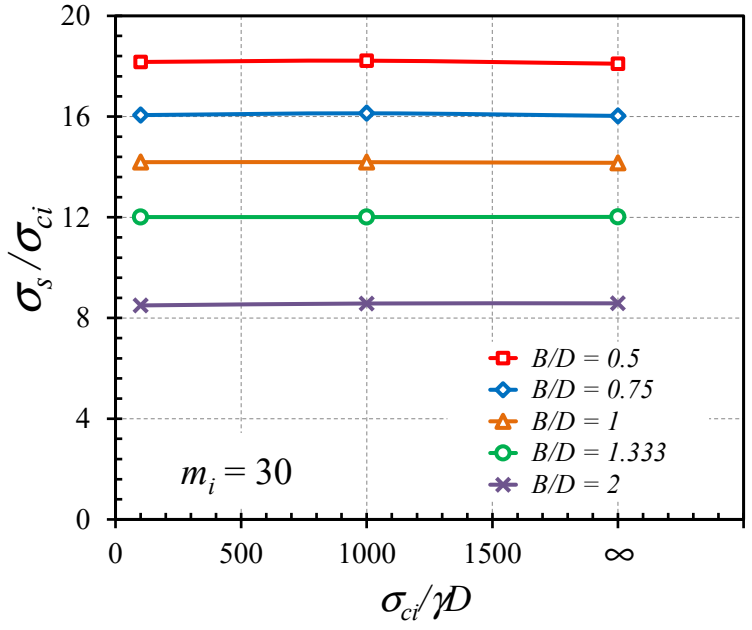

(**b**)

Figure 6. Impact of $\sigma_{ci}/\gamma D$ on σ_s/σ_{ci} of horseshoe tunnels with C/D = 3 and GSI = 80: (**a**) m_i = 5 and (**b**) m_i = 30.

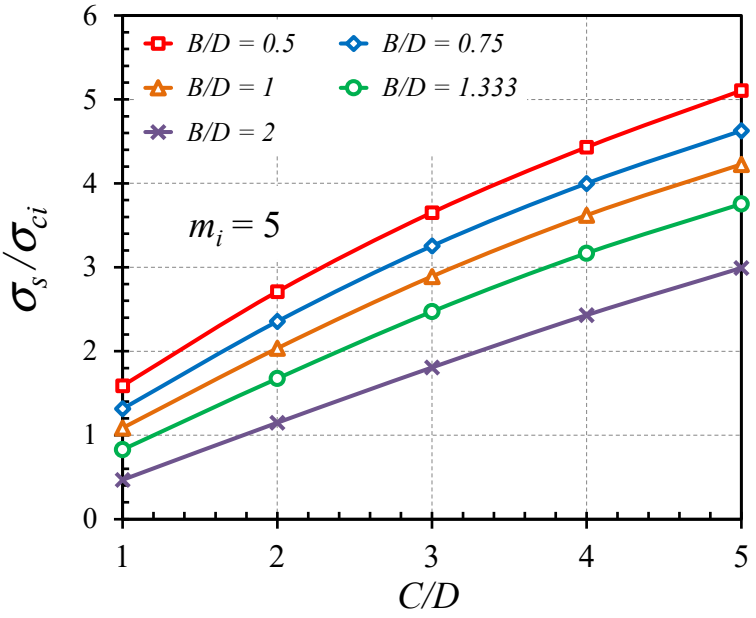

(**a**)

Figure 7. *Cont.*

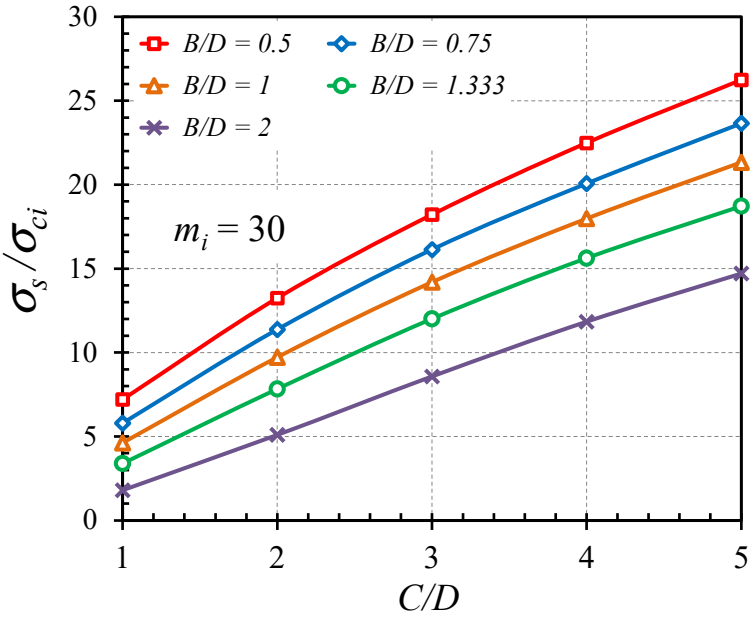

(**b**)

Figure 7. Impact of C/D on σ_s/σ_{ci} of horseshoe tunnels with $\sigma_{ci}/\gamma D = 1000$ and $GSI = 80$: (**a**) $m_i = 5$ and (**b**) $m_i = 30$.

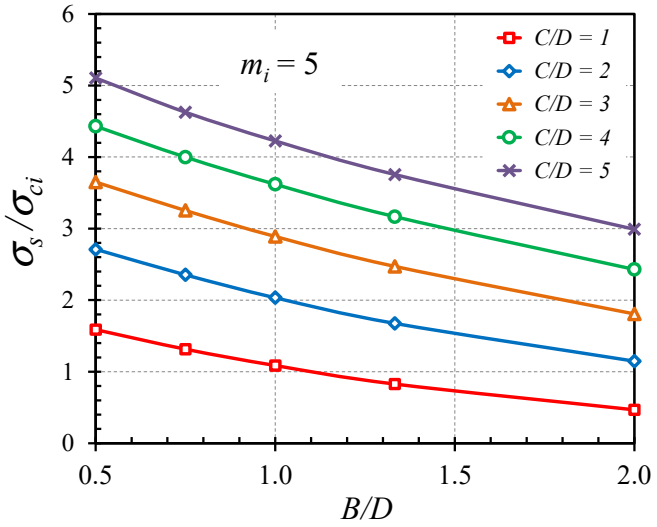

(**a**)

Figure 8. *Cont.*

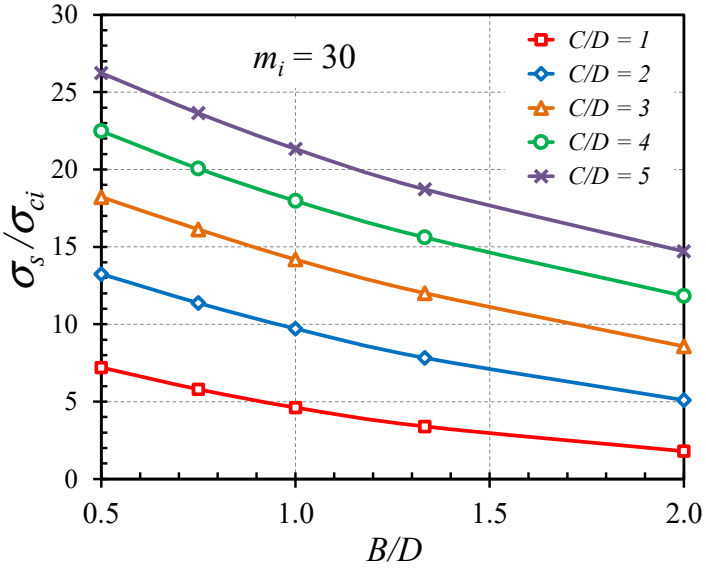

(**b**)

Figure 8. Impact of B/D on σ_s/σ_{ci} of horseshoe tunnels with $\sigma_{ci}/\gamma D$ = 1000 and GSI = 80: (**a**) m_i = 5 and (**b**) m_i = 30.

The influence of the GSI on the stability factor σ_s/σ_{ci} can be seen Figure 4a,b within the case of m_i = 5 and 30. The representing figure is drawn based on the instances of C/D = 3 and $\sigma_{ci}/\gamma D$ = 1000. Five selected various width ratios of B/D = 0.5, 0.75, 1, 1.333, and 2 are also plotted in the figures. According to numerical findings, the relationship between the GSI and σ_s/σ_{ci}, are formed exponentially, while an increase in the GSI leading to a nonlinear increase in σ_s/σ_{ci} for all ranges of B/D. These outcomes may be attributed to the exponential function utilized in the HB-failure-criterion model and represented in Equations (2)–(4). In fact, a high GSI value indicates a rock mass that has not been significantly disturbed, which raises the stability of rock tunnels.

The impact of m_i on σ_s/σ_{ci} for the GSI = 40 and 100 is shown in Figure 5a,b, respectively. The plots contain five distinct width ratios of B/D = 0.5, 0.75, 1, 1.333, and 2 and are established using the chosen parameters of C/D = 3 and $\sigma_{ci}/\gamma D$ = 1000. Based on the obtained results, it is clearly observed that m_i directly affects σ_s/σ_{ci} in the positive linear variation pattern. For all B/D ranges, a rise in m_i leads to a rise in σ_s/σ_{ci}. Generally, m_i is determined by the mineralogy, composition, and grain size of the intact rock mass in physical aspect.

The impact of $\sigma_{ci}/\gamma D$ on σ_s/σ_{ci} is shown in Figure 6a,b, since all the data are shown only in a linear horizontal relation, demonstrating that the rise in $\sigma_{ci}/\gamma D$ has no impact on the σ_s/σ_{ci} values. This finding applies to all B/D, m_i and the GSI values. The total rock tunnel stability is seldom affected by the unit weight ratio of $\sigma_{ci}/\gamma D$ since, in this study, we defined the value of σ_{ci} to be very large comparing to that of γD, where the considered range of is $\sigma_{ci}/\gamma D$ = 100–∞. However, the cases with $\sigma_{ci}/\gamma D$ being less than 100 are beyond the scope of this study. More studies on those cases with small values of $\sigma_{ci}/\gamma D$ being less than 100 should be carried out in the future.

The impact of the cover-depth ratio C/D on σ_s/σ_{ci} for the cases of ($\sigma_{ci}/\gamma D$ = 1000, GSI = 80 and m_i = 5 and 30) are shown in Figure 7a,b respectively, in which it is demonstrated that C/D and σ_s/σ_{ci} have a nonlinear increasing relationship, while an increase in the C/D value leads to a higher value of the stability factor σ_s/σ_{ci}. It may be explained by the typical phenomenon that the deeper the tunnel is, the greater stability can be achieved. Figure 8a,b show the impact of B/D on σ_s/σ_{ci} for the cases of ($\sigma_{ci}/\gamma D$ = 1000 and GSI = 80 and m_i = 5 and 30). It can be understood that the geometrical arching effect would develop with either a rise in C/D or a fall in B/D, which would be advantageous for enhancing the

tunnel stability. Numerical results of all C/D values show that when B/D increases, σ_s/σ_{ci} also increases non-linearly. Also, a higher B/D ratio yields a lesser value of σ_s/σ_{ci}.

5.3. Failure Mechanisms

The final adaptive meshes using the 5th iteration for the three B/D = 0.5, 1, and 2 are shown in Figure 9, while the plots of the shear dissipations indicating the failure zones of the three B/D are presented Figure 10. These plots are based on the case of ($\sigma_{ci}/\gamma D$ = 1000, GSI = 80, and m_i = 20). It is interesting to note that either the final adaptive meshes or the shear dissipation plots are adapted to represent the plastic shear zone of the horseshoe tunnels in rock masses. Note that the zones with the adaptive mesh refinement can be used to represent the same zones of the shear dissipation since the patterns of both are in the similar manner. The failure zone frequently displayed an oval form and spans from the tunnel's base to the rock's surface. The size of the failure zone around the tunnel is reduced by a greater B/D. The failure zone for the case with B/D = 2.0 extends from the corner point of the tunnel, while the failure zone for the case with B/D = 0.5 extends from below the base of tunnel.

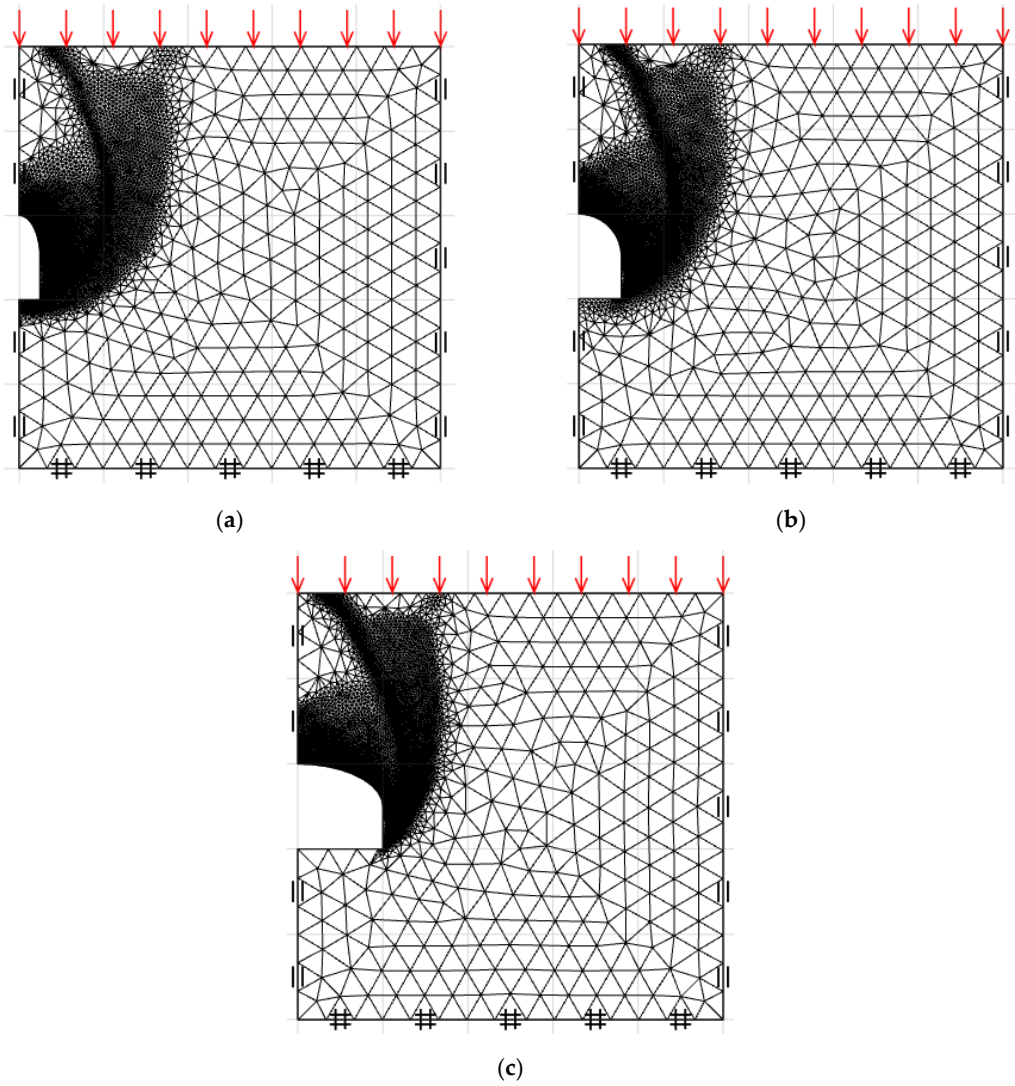

Figure 9. Final adaptive meshes of horseshoe tunnel: (**a**) B/D = 0.5, (**b**) B/D = 1 and (**c**) B/D = 2 (GSI = 80, C/D = 2, $\sigma_{ci}/\gamma D$ = 1000, and m_i = 20).

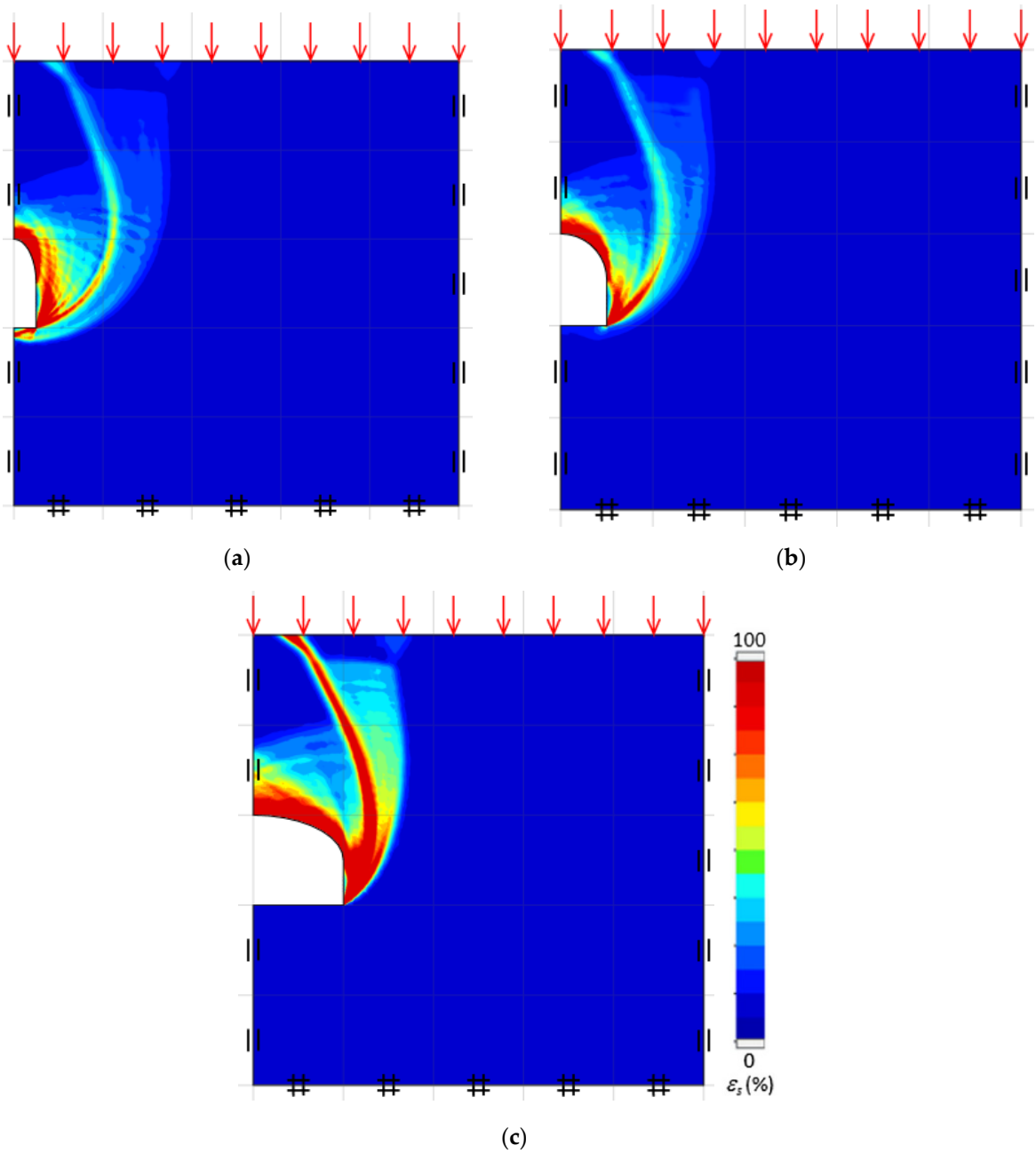

Figure 10. Shear dissipations of horseshoe tunnel: (**a**) B/D = 0.5, (**b**) B/D = 1 and (**c**) B/D = 2 (GSI = 80, C/D = 2, $\sigma_{ci}/\gamma D$ = 1000, and m_i = 20).

Figure 11 presents the failure mechanisms for the four GSI values while the plots in Figure 12 are for four different m_i values. The chosen cases for Figure 11 are (C/D = 2, B/D = 0.5, $\sigma_{ci}/\gamma D$ = 1000, m_i = 20, and GSI = 40, 60, 80, and 100), whereas Figure 12 shows the cases of (C/D = 2, B/D = 2, $\sigma_{ci}/\gamma D$ = 1000, GSI = 80, and m_i = 5, 10, 20, 30). From both figures, it can be concluded that the influence of the GSI and m_i on the overall failure mechanisms is negligible, given the uniform surcharge pressures at the collapse state. The absolute values of shear dissipation are not significant; hence, they are not shown in the figures.

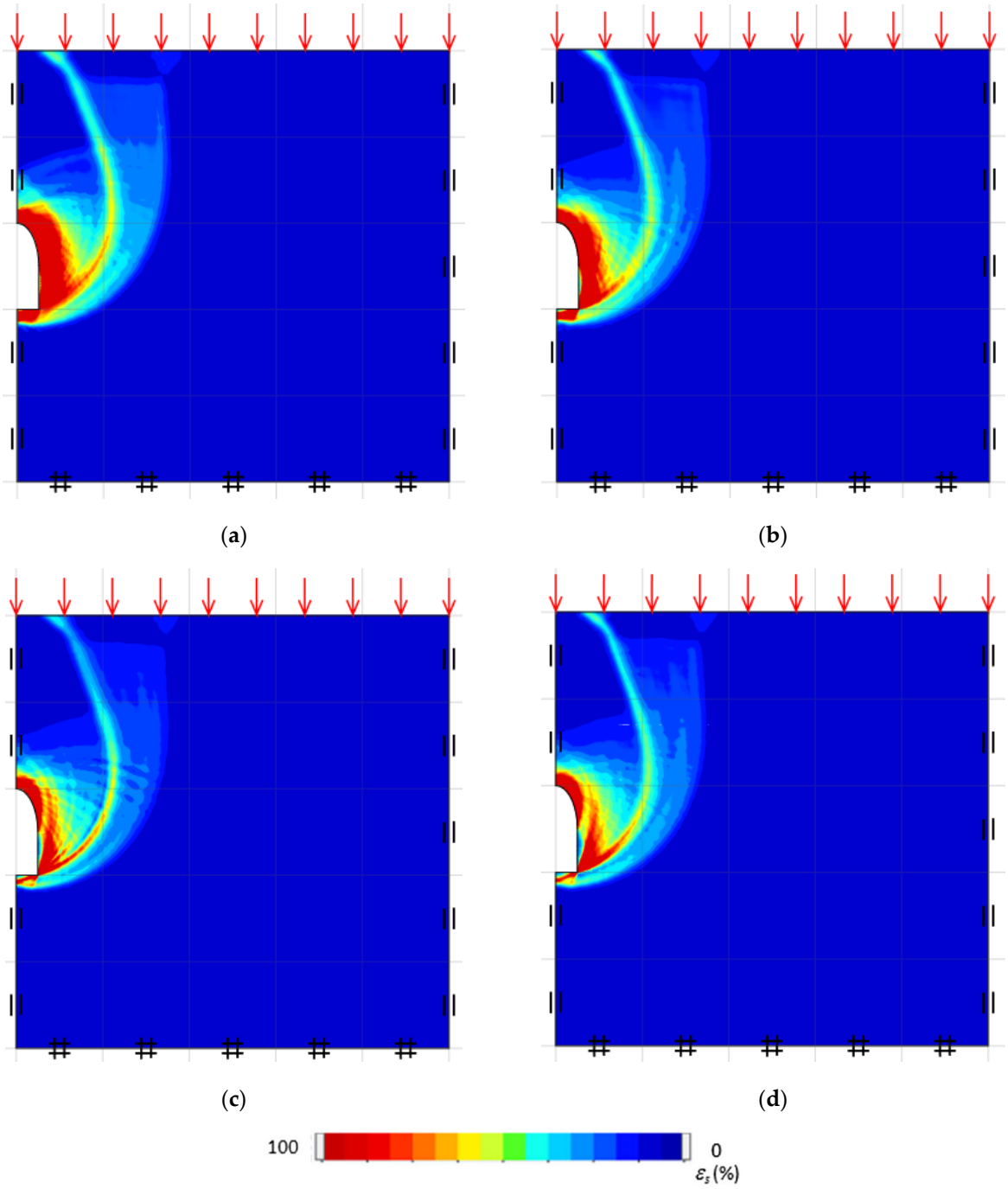

Figure 11. Shear dissipations for various *GSI*: (**a**) 40, (**b**) 60, (**c**) 80 and (**d**) 100 (C/D = 2, B/D = 0.5, $\sigma_{ci}/\gamma D$ = 1000 and m_i = 20).

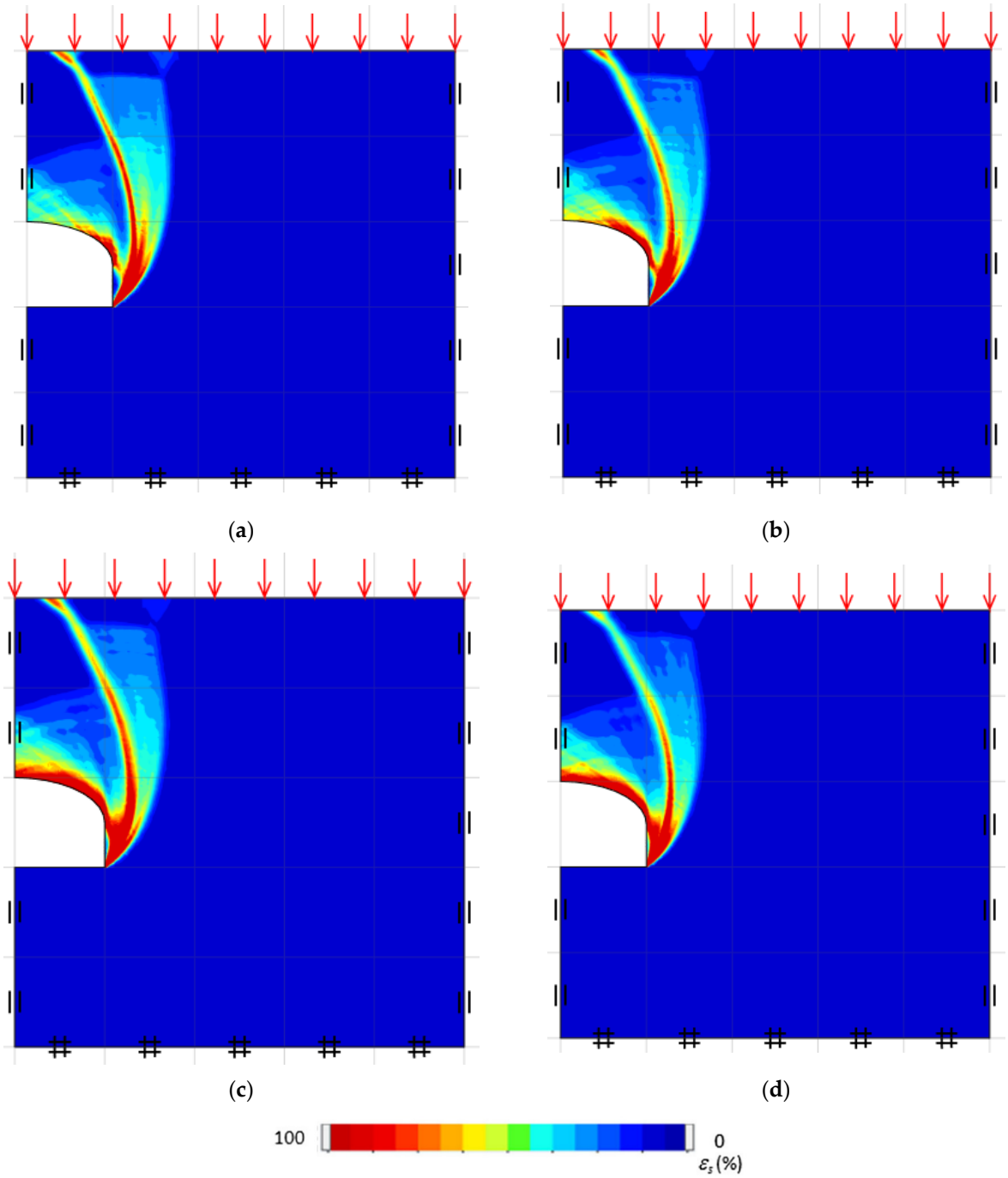

Figure 12. Shear dissipations for various m_i: (**a**) 5, (**b**) 10, (**c**) 20 and (**d**) 30 (C/D = 2, B/D = 2, $\sigma_{ci}/\gamma D$ = 1000 and GSI = 80).

Figures 13–15 show the failure mechanisms that have been affected by the cover-depth ratio for B/D = 0.5, 1, and 2, respectively. Other parameters are fixed as: $\sigma_{ci}/\gamma D$ = 1000, GSI = 80, and m_i = 20. In general, the failure mechanisms resemble each other under the uniform surcharge effects. It is also important to note the three possible slip planes; one is above the tunnel and the other two spiral upwards to the ground level from the tunnels side. The failure zone spreads further away from the tunnel as C/D is increased.

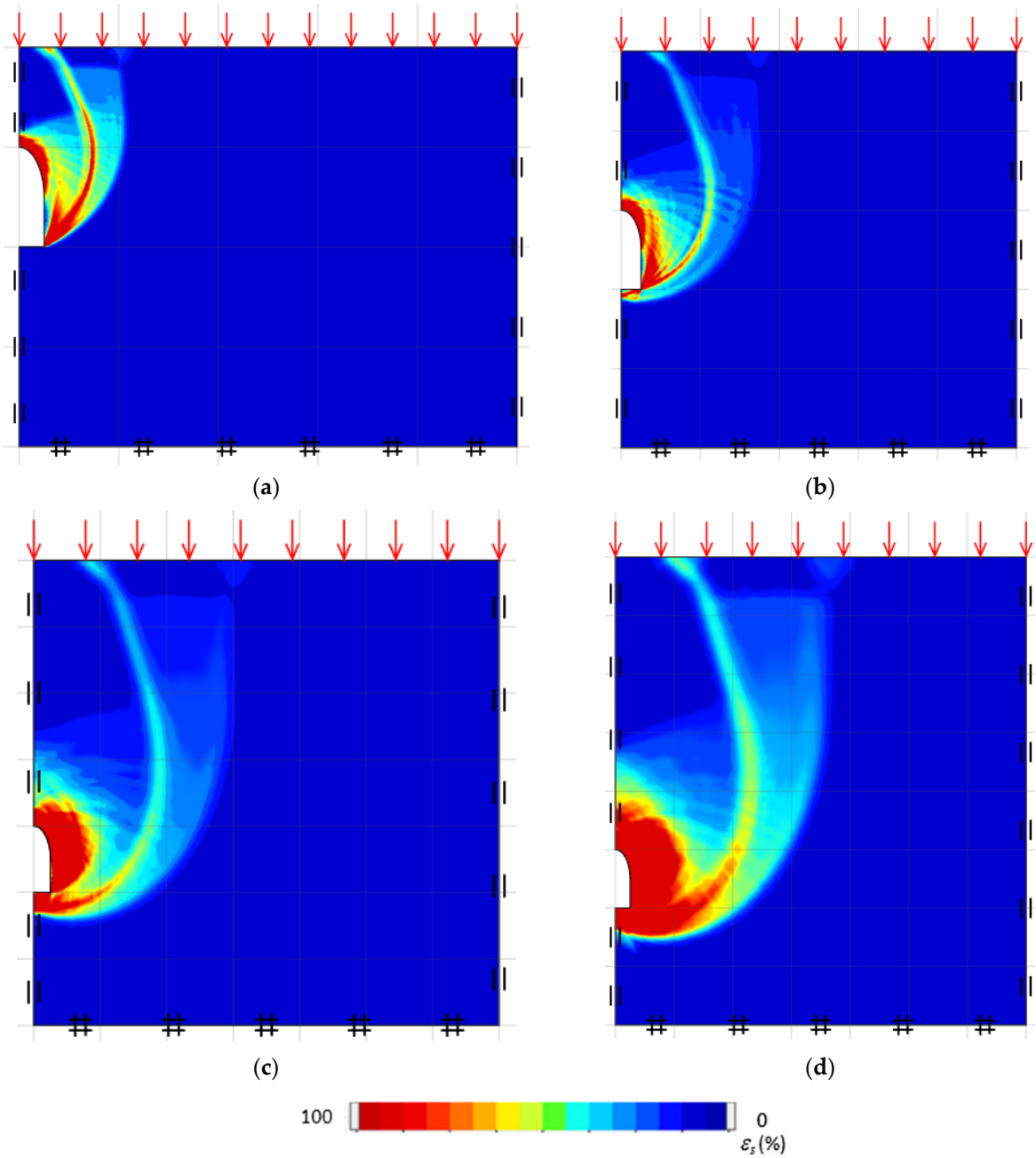

Figure 13. Shear dissipations of horseshoe tunnel with B/D = 0.5 for the cases of C/D: (**a**) 1, (**b**) 2, (**c**) 4 and (**d**) 5 ($\sigma_{ci}/\gamma D$ = 1000, GSI = 80 and m_i = 20).

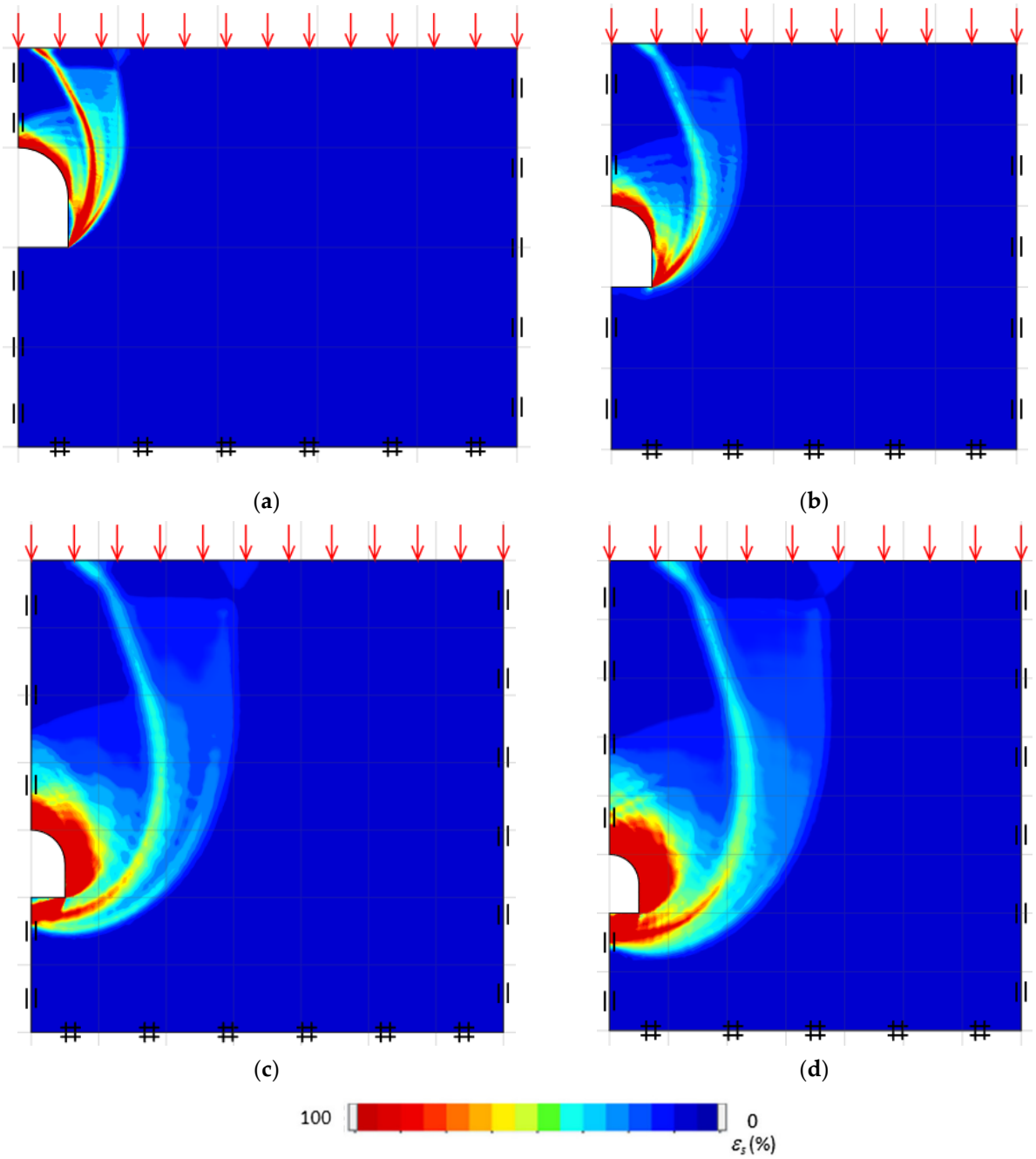

Figure 14. Shear dissipations of horseshoe tunnel with B/D = 1 for the cases of C/D: (**a**) 1, (**b**) 2, (**c**) 4 and (**d**) 5 ($\sigma_{ci}/\gamma D$ = 1000, GSI = 80 and m_i = 20).

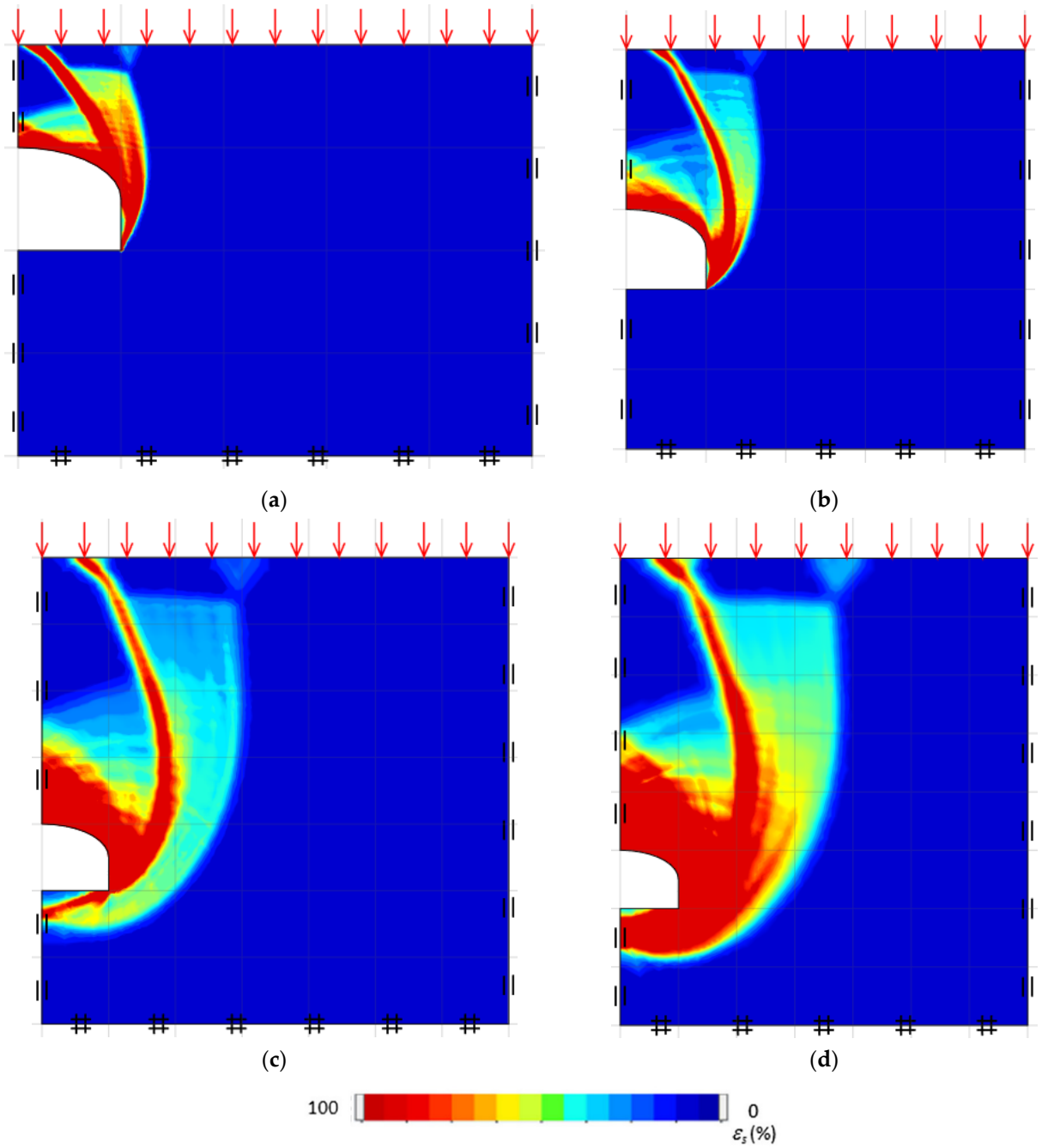

Figure 15. Shear dissipations of unlined horseshoe tunnel in rock mass with B/D = 2 for the cases of C/D: (**a**) 1, (**b**) 2, (**c**) 4 and (**d**) 5 ($\sigma_{ci}/\gamma D$ = 1000, GSI = 80 and m_i = 20).

5.4. Comparison among Different Tunnel Shapes

Figure 16 presents a comparison of the stability factors σ_s/σ_{ci} among various tunnel forms. Figure 16a,b are related to m_i = 5 and m_i = 30, respectively. Some published papers for the similar problem are carried out in the comparison including the problems of a plane strain tunnel heading [41], a square tunnel [37], and a circular tunnel [34]. The current horseshoe tunnel problems (B/D = 0.5, 1, and 2) are compared to all of the above studies. According to numerical data in Figure 16, the greatest stability factor σ_s/σ_{ci} among the six varied forms is the result of the planar tunnel headings. The lowest stability factor can be founded in the cases of the horseshoe tunnel with a large B/D value (B/D = 2) due to the large unsupported width of the tunnel. This comparison is useful in determining the form

of a tunnel. Furthermore, it may be used to validate the current solution since it exhibits the identical pattern as earlier studies.

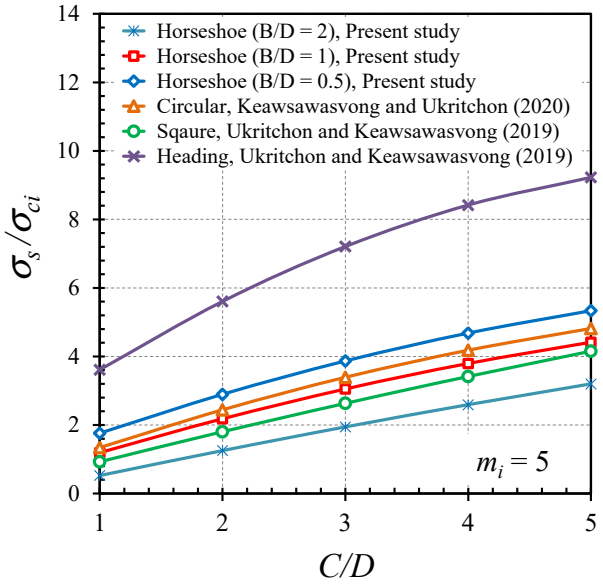

(**a**)

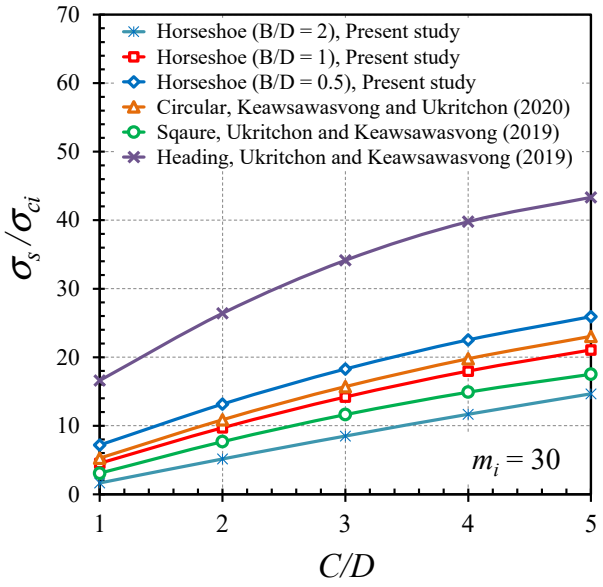

(**b**)

Figure 16. Comparison of the stability factors σ_s/σ_{ci} for different shapes of tunnels: (**a**) m_i = 5 and (**b**) m_i = 30 ($\sigma_{ci}/\gamma D$ = 1000 and GSI = 80 Design equations.

According to Equation (5) and Figures 4–8, σ_s/σ_{ci}, the results of the tunnel stability depend on a number of dimensionless parameters, such as B/D, C/D, GSI, m_i, and $\sigma_{ci}/\gamma D$. Given that in the current investigation the discrepancies between the calculated UB and LB solutions are under 5%, their average (Ave) values were used to develop the design equations. In order to achieve the mathematical equations, the authors attempted numerous curve-fitting techniques on the Ave solutions. As a result, it can be summarized that extremely strong correlations exists between σ_s/σ_{ci} and a linear function of $\gamma D/\sigma_{ci}$, a cubic

function of the GSI, a linear function of m_i, and a quadratic function of C/D, as expressed as follows:

$$\frac{\sigma_s}{\sigma_{ci}} = A_1 + A_2\left(\frac{C}{D}\right) + A_3\left(\frac{C}{D}\right)^2 \tag{6a}$$

$$\frac{\sigma_s}{\sigma_{ci}} = B_1 + B_2(GSI) + B_3(GSI)^2 + B_4(GSI)^3 \tag{6b}$$

$$\frac{\sigma_s}{\sigma_{ci}} = E_1 + E_2(m_i) \tag{6c}$$

$$\frac{\sigma_s}{\sigma_{ci}} = G_1 + G_2\left(\frac{\gamma D}{\sigma_{ci}}\right) \tag{6d}$$

where A_i, B_i, E_i, G_i are coefficients from the curve-fitting method for the different dimensionless parameters.

By combining all expression in Equation (6) in the equations with the best mathematic forms, the design equations for computing σ_s/σ_{ci} are developed and expressed in Equations (7a)–(7d):

$$\frac{\sigma_s}{\sigma_{ci}} = F_1 + F_2 m_i - F_3\left(\frac{\gamma D}{\sigma_{ci}}\right) \tag{7a}$$

$$F_1 = GSI\left[b_1 + b_2\frac{C}{D} + b_3\left(\frac{C}{D}\right)^2\right] + GSI^2\left[c_1 + c_2\frac{C}{D} + c_3\left(\frac{C}{D}\right)^2\right] \tag{7b}$$

$$F_2 = e_1 + e_2\frac{C}{D} + GSI\left[f_1 + f_2\frac{C}{D} + f_3\left(\frac{C}{D}\right)^2\right] + GSI^2\left[g_1 + g_2\frac{C}{D}\right] + GSI^3\left(d_1\frac{C}{D}\right) \tag{7c}$$

$$F_3 = a_1 + a_2\frac{C}{D} \tag{7d}$$

where a_i, b_i, c_i, d_i, e_i, f_i, and g_i in Equations (7a)–(7d) denote the constant coefficients.

The least squares approach is a straightforward method to resolve the seven constant coefficients given in Equation (7) [59] by reducing the squared sum of the deviation in σ_s/σ_{ci} between the FELA and the approximate solutions, which can be seen as follows [59]:

$$Minimize\left(error^2\right) = Minimize\left(\sum_{i=1}^{n}(y_i - f_i)^2\right) \tag{8}$$

where y_i = Ave FELA solutions

f_i = Approximate solutions of σ_s/σ_{ci} from Equation (7a)

n = Number of data

The accuracy of the proposed new design equation can be verified using the coefficient of determination, R^2 as [59]:

$$R^2 = 1 - \frac{SS_{res}}{SS_{tot}} \tag{9a}$$

$$SS_{tot} = \sum_{i=1}^{n}(y_i - \overline{y})^2 \tag{9b}$$

$$SS_{res} = \sum_{i=1}^{n}(y_i - f_i)^2 \tag{9c}$$

$$\overline{y} = \frac{1}{n}\sum_{i=1}^{n}(y_i) \tag{9d}$$

Using the aforesaid approach, Table 2 provides all the constants required in the proposed stability equations. For all B/D values, there is a strong correlation between the predictions and the Ave solutions. Note that the coefficient of determination (R^2) is 99.98% for all B/D. Note that the value of R^2 can be computed from Equation (9) by employing

all Ave FELA solutions (y_i) and all approximate solutions from Equation (7a) (f_i) with the value of n = 1200 cases so that the value of R^2 is then obtained. Hence, the proposed design Equation (7) can be used with great confidence in predicting the collapse surcharges σ_s/σ_{ci} of shallow unlined horseshoe tunnels in Hoek–Brown rock masses.

Table 2. Optimal value of the constants for the design equation (B/D = 0.5 to 2.0).

Constants	*B/D*				
	0.50	**0.75**	**1.00**	**1.33**	**2.00**
a_1	-1.1961	-0.7953	0.7507	0.0739	-0.9954
a_2	-1.0018	-1.1190	1.0521	-0.1071	-1.6162
b_1	0.0227	0.0217	0.0196	0.0151	0.4874×10^{-2}
b_2	-0.0325	-0.03018	-0.0275	-0.0216	-0.0100
b_3	0.0049	0.4442×10^{-2}	0.3960×10^{-2}	0.3004×10^{-2}	0.1119×10^{-2}
c_1	-0.2074×10^{-3}	-0.2083×10^{-3}	-0.1888×10^{-3}	-0.1413×10^{-3}	-0.0435×10^{-3}
c_2	0.4371×10^{-3}	0.4092×10^{-3}	0.3700×10^{-3}	0.2950×10^{-3}	0.1562×10^{-3}
c_3	-0.6221×10^{-4}	-0.5704×10^{-4}	-0.5019×10^{-4}	-0.3764×10^{-4}	-0.1514×10^{-4}
d_1	1.2130×10^{-6}	1.07167×10^{-6}	9.7466×10^{-7}	8.3863×10^{-7}	0.6487×10^{-6}
e_1	0.1421	0.0984	0.0575	0.0173	-0.0394
e_2	-0.1718	-0.1431	-0.1245	-0.0974	-0.0633
f_1	-0.6318×10^{-2}	-0.4631×10^{-2}	-0.3009×10^{-2}	-0.1292×10^{-2}	0.1305×10^{-2}
f_2	0.0115	0.9847×10^{-2}	0.8725×10^{-2}	0.7073×10^{-2}	0.4704×10^{-2}
f_3	-0.1756×10^{-3}	-0.1616×10^{-3}	-0.1436×10^{-3}	-0.1104×10^{-3}	-0.0326×10^{-3}
g_1	0.5601×10^{-4}	0.3712×10^{-4}	0.1968×10^{-4}	0.2055×10^{-5}	0.2130×10^{-4}
g_2	-0.1766×10^{-3}	-0.1522×10^{-3}	-0.1360×10^{-3}	-0.1129×10^{-3}	-0.0822×10^{-3}
R^2	99.98%	99.98%	99.98%	99.98%	99.98%

5.5. Example

The dimensions of a horseshoe tunnel are defined as B = 6 m horizontally, D = 3 m vertically, and C = 3 m cover depth. The rock mass profile is set by several geotechnical properties including the GSI = 50, m_i = 17, σ_{ci} = 63 MPa, and γ = 22 kN/m^3. Figure out the maximum surcharge (σ_t) that can cause the collapse of the tunnel.

1. Calculate all the values B/D = 6/3 = 2, C/D = 3/3 = 1, and $\gamma D/\sigma_{ci}$ = 22*3/63,000 = 0.001.
2. According to B/D = 2, the values of all constant coefficients including a_1, a_2, b_1, b_2, b_3, c_1, c_2, c_3, d_1, e_1, e_2, f_1, f_2, f_3, g_1, and g_2 from Table 2 are then obtained.
3. Substitute the values of all the parameters such as C/D, $\gamma D/\sigma_{ci}$, the GSI, m_i, and a_1 to g_2 into Equations 7(a)-7(d); then, σ_s/σ_{ci} can be obtained as: σ_s/σ_{ci} = 0.353.
4. Calculate σ_s = 63*0.353 = 22.24 MPa.

6. Conclusions

The objective of this paper is to provide the stability charts and equations for the unlined horseshoe rock tunnel problem based on the Hoek–Brown model. The stability solutions were determined for an extensive range of dimensionless parameters by the finite-element-limit analysis. These may include the width ratio B/D of 0.5–2, and the m_i parameter of 5–30 the cover-depth ratio C/D of 1–5, the geological strength index GSI of 40–100 and the normalized uniaxial compressive strength $\sigma_{ci}/\gamma D$ of 100-∞. In brief, all of the studies described above come to the following conclusions:

- The derived upper and lower bound can surround the genuine solutions below 5% of their average values while applying the adaptive meshing approach.
- The influence of m_i and $\gamma D/\sigma_{ci}$ on the normalized failure surcharge σ_s/σ_{ci} is a linear relationship whereas that of B/D, C/D, and the GSI is a nonlinear relationship.
- Regarding the failure mechanisms, it was found that the influence of the GSI and m_i on the overall failure mechanisms is neglectable. A horseshoe tunnel with a large

value of B/D or C/D has a greater failure zone that penetrates extensively and deeply through the rock masses.

- A comparison of the stability factor σ_s/σ_{ci} for various tunnel shapes was also presented in the study. It was found that the greatest stability factor is observed in the instance of the plane strain heading, in descending order with the horseshoe tunnel with $B/D = 0.5$, the circular tunnel, the horseshoe tunnel with $B/D = 1$, the square tunnel, and the horseshoe tunnel with $B/D = 2$.
- Utilizing the computed average bound solutions, the novel stability equations are established for predicting the stability factor σ_s/σ_{ci}. The suggested design equations' accuracy is demonstrated by their coefficient of determination $R^2 = 99.98\%$. These equations can be used with confidence in design practice.

Author Contributions: J.L.: Data curation, Software, Investigation, Methodology, Writing—original draft; J.S.: Methodology, Writing—review & editing, Supervision; S.K.: Methodology, Validation, Writing –original draft; S.S.: Formal analysis, Software, Methodology; P.J.: Writing—review, revising & editing, Project administration, Supervision, Funding acquisition. All authors have read and agreed to the published version of the manuscript.

Funding: This research was funded by the National Science, Research and Innovation Fund (NSRF), and King Mongkut's University of Technology North Bangkok with Contract no. KMUTNB-FF-65-38.

Data Availability Statement: All data, models, or code that support the findings of this study are available from the corresponding author upon reasonable request.

Conflicts of Interest: The authors declare that they have no known competing financial interests or personal relationships that could have appeared to influence the work reported in this paper.

References

1. Kirsch, A. Experimental investigation of the face stability of shallow tunnels in sand. *Acta Geotech.* **2010**, *5*, 43–62. [CrossRef]
2. Chambon, P.; Corté, J.F. Shallow tunnels in cohesionless soil: Stability of tunnel face. *J. Geotech. Eng.* **1994**, *120*, 1148–1165. [CrossRef]
3. Kimura, T.; Mair, R.J. Centrifugal testing of model tunnels in soft clay. In Proceedings of the 10th International Conference on Soil Mechanics and Foundation Engineering, Stockholm, Sweden, 15–19 June 1981; pp. 319–322.
4. Davis, E.H.; Gunn, M.J.; Mair, R.J.; Seneviratine, H.N. The stability of shallow tunnels and underground openings in cohesive material. *Géotechnique* **1980**, *30*, 397–416. [CrossRef]
5. Sloan, S.W. Geotechnical stability analysis. *Géotechnique* **2013**, *63*, 531–572. [CrossRef]
6. Shiau, J.; Al-Asadi, F. Revisiting Broms and Bennermarks' original stability number for tunnel headings. *Géotechnique Lett.* **2018**, *8*, 310–315. [CrossRef]
7. Wilson, D.W.; Abbo, A.J.; Sloan, S.W.; Lyamin, A.V. Undrained stability of a circular tunnel where the shear strength increases linearly with depth. *Can. Geotech. J.* **2011**, *48*, 1328–1342. [CrossRef]
8. Yamamoto, K.; Lyamin, A.V.; Wilson, D.W.; Sloan, S.W.; Abbo, A.J. Stability of a circular tunnel in cohesive-frictional soil subjected to surcharge loading. *Comput. Geotech.* **2011**, *38*, 504–514. [CrossRef]
9. Assadi, A.; Sloan, S.W. Undrained stability of shallow square tunnel. *J. Geotech. Eng.* **1991**, *117*, 1152–1173. [CrossRef]
10. Sloan, S.W.; Assadi, A. Undrained stability of a square tunnel in a soil whose strength increases linearly with depth. *Comput. Geotech.* **1991**, *12*, 321–346. [CrossRef]
11. Ukritchon, B.; Keawsawasvong, S. Undrained stability of unlined square tunnels in clays with linearly increasing anisotropic shear strength. *Geotech. Geol. Eng.* **2020**, *38*, 897–915. [CrossRef]
12. Wilson, D.W.; Abbo, A.J.; Sloan, S.W.; Lyamin, A.V. Undrained stability of a square tunnel where the shear strength increases linearly with depth. *Comput. Geotech.* **2013**, *49*, 314–325. [CrossRef]
13. Yamamoto, K.; Lyamin, A.V.; Wilson, D.W.; Sloan, S.W.; Abbo, A.J. Stability of a single tunnel in cohesive–frictional soil subjected to surcharge loading. *Can. Geotech. J.* **2011**, *48*, 1841–1854. [CrossRef]
14. Augarde, C.E.; Lyamin, A.V.; Sloan, S.W. Stability of an undrained plane strain heading revisited. *Comput. Geotech.* **2003**, *30*, 419–430. [CrossRef]
15. Sloan, S.W.; Assadi, A. Undrained stability of a plane strain heading. *Can. Geotech. J.* **1994**, *31*, 443–450. [CrossRef]
16. Ukritchon, B.; Keawsawasvong, S. Lower bound solutions for undrained face stability of plane strain tunnel heading in anisotropic and non-homogeneous clays. *Comput. Geotech.* **2019**, *112*, 204–217. [CrossRef]
17. Sirimontree, S.; Keawsawasvong, S.; Ngamkhanong, C.; Seehavong, S.; Sangjinda, K.; Jearsiripongkul, T.; Thongchom, C.; Nuaklong, P. Neural network-based prediction model for the stability of unlined elliptical tunnels in cohesive-frictional soils. *Building* **2022**, *12*, 444. [CrossRef]

18. Keawsawasvong, S.; Shiau, J. Stability of active trapdoors in axisymmetry. *Undergr. Space* **2022**, *7*, 50–57. [CrossRef]
19. Ukritchon, B.; Keawsawasvong, S.; Yingchaloenkitkhajorn, K. Undrained face stability of tunnels in Bangkok Subsoils. *Int. J. Geotech. Eng.* **2017**, *11*, 262–277. [CrossRef]
20. Keawsawasvong, S.; Ukritchon, B. Design equation for stability of a circular tunnel in an anisotropic and heterogeneous clay. *Undergr. Space* **2022**, *7*, 76–93. [CrossRef]
21. Shiau, J.; Keawsawasvong, S. Producing undrained stability factors for various tunnel shapes. *Int. J. Geomech.* **2022**, *22*, 06022017. [CrossRef]
22. Ukritchon, B.; Keawsawasvong, S. Design equations for undrained stability of opening in underground walls. *Tunn. Undergr. Space Technol.* **2017**, *70*, 214–220. [CrossRef]
23. Ukritchon, B.; Keawsawasvong, S. Stability of retained soils behind underground walls with an opening using lower bound limit analysis and second-order cone programming. *Geotech. Geol. Eng.* **2019**, *37*, 1609–1625. [CrossRef]
24. Wilson, D.W.; Abbo, A.J.; Sloan, S.W. Undrained stability of tall tunnels. In *Computer Methods and Recent Advances in Geomechanics*; Oka, F., Murakami, A., Uzuoka, R., Kimoto, S., Eds.; CRC Press: Boca Raton, FL, USA, 2014; pp. 447–452.
25. Bhattacharya, P.; Sriharsha, P. Stability of horseshoe tunnel in cohesive-frictional soil. *Int. J. Geomech.* **2020**, *20*, 06020021. [CrossRef]
26. Zhang, J.; Feng, T.; Yang, J.; Feng, Y.; Gao, Y. Upper-bound stability analysis of dual unlined horseshoe-shaped tunnels subjected to gravity. *Comput. Geotech.* **2018**, *97*, 103–110. [CrossRef]
27. Sun, R.; Yang, J.; Liu, S.; Yang, F. Undrained stability analysis of dual unlined horseshoe-shaped tunnels in non-homogeneous clays using lower bound limit analysis method. *Comput. Geotech.* **2021**, *133*, 104057. [CrossRef]
28. Mollon, G.; Dias, D.; Soubra, A.H. Rotational failure mechanisms for the face stability analysis of tunnels driven by a pressurized shield. *Int. J. Numer. Anal. Methods Geomech.* **2011**, *35*, 1363–1388. [CrossRef]
29. Zhang, C.; Han, K.; Zhang, D. Face stability analysis of shallow circular tunnels in cohesive-frictional soils. *Tunn. Undergr. Space Technol.* **2015**, *50*, 345–357. [CrossRef]
30. Zhang, C.; Li, W.; Zhu, W.; Tan, Z. Face stability analysis of a shallow horseshoe-shaped shield tunnel in clay with a linearly increasing shear strength with depth. *Tunn. Undergr. Space Technol.* **2020**, *97*, 103291. [CrossRef]
31. Jearsiripongkul, T.; Keawsawasvong, S.; Banyong, R.; Seehavong, S.; Sangjinda, K.; Thongchom, C.; Chavda, J.; Ngamkhanong, C. Stability evaluations of unlined horseshoe tunnels based on extreme learning neural network. *Computation* **2022**, *10*, 81. [CrossRef]
32. Li, W.; Zhang, C.; Zhu, W.; Zhang, D. Upper-bound solutions for the face stability of a non-circular NATM tunnel in clays with a linearly increasing undrained shear strength with depth. *Comput. Geotech.* **2019**, *114*, 103136. [CrossRef]
33. Hoek, E.; Brown, E.T. Empirical strength criterion for rock masses. *J. Geotech. Eng. Div.* **1980**, *106*, 1013–1035. [CrossRef]
34. Keawsawasvong, S.; Ukritchon, B. Design equation for stability of shallow unlined circular tunnels in Hoek-Brown rock masses. *Bull. Eng. Geol. Environ.* **2020**, *79*, 4167–4190. [CrossRef]
35. Zhang, R.; Xiao, Y.; Zhao, M.; Zhao, H. Stability of dual circular tunnels in a rock mass subjected to surcharge loading. *Comput. Geotech.* **2019**, *108*, 257–268. [CrossRef]
36. Farhadian, H. A new empirical chart for rockburst analysis in tunnelling: Tunnel rockburst classification (TRC). *Int. J. Min. Sci. Technol.* **2021**, *31*, 603–610. [CrossRef]
37. Ukritchon, B.; Keawsawasvong, S. Stability of unlined square tunnels in Hoek-Brown rock masses based on lower bound analysis. *Comput. Geotech.* **2019**, *105*, 249–264. [CrossRef]
38. Xiao, Y.; Zhao, M.; Zhang, R.; Zhao, H.; Wu, G. Stability of dual square tunnels in rock masses subjected to surcharge loading. *Tunn. Undergr. Space Technol* **2019**, *92*, 103037. [CrossRef]
39. Xiao, Y.; Zhang, R.; Zhao, M.; Jiang, J. Stability of unlined rectangular tunnels in rock masses subjected to surcharge loading. *Int. J. Geomech.* **2021**, *21*, 04020233. [CrossRef]
40. Rahaman, O.; Kumar, J. Stability analysis of twin horse-shoe shaped tunnels in rock mass. *Tunn. Undergr. Space Technol* **2020**, *98*, 103354. [CrossRef]
41. Ukritchon, B.; Keawsawasvong, S. Lower bound stability analysis of plane strain headings in Hoek-Brown rock masses. *Tunn. Undergr. Space Technol.* **2019**, *84*, 99–112. [CrossRef]
42. Hoek, E.; Carranza-Torres, C.; Corkum, B. Hoek–Brown failure criterion—2002 edition. In Proceedings of the 5th North American Rock Mechanics Symposium, Toronto, ON, Canada, 7–10 July 2002.
43. OptumCE. OptumG2. *Optum Computational Engineering: Copenhagen, Denmark*. 2020. Available online: https://optumce.com/ (accessed on 1 February 2022).
44. Ciria, H.; Peraire, J.; Bonet, J. Mesh adaptive computation of upper and lower bounds in limit analysis. *Int. J. Numer. Methods Eng.* **2008**, *75*, 899–944. [CrossRef]
45. Yodsomjai, W.; Keawsawasvong, S.; Senjuntichai, T. Undrained stability of unsupported conical slopes in anisotropic clays based on Anisotropic Undrained Shear failure criterion. *Transp. Infrastruct. Geotechnol.* **2021**, *8*, 557–568.
46. Yodsomjai, W.; Keawsawasvong, S.; Thongchom, C.; Lawongkerd, J. Undrained stability of unsupported conical slopes in two-layered clays. *Innov. Infrastruct. Solut.* **2021**, *6*. [CrossRef]
47. Yodsomjai, W.; Keawsawasvong, S.; Likitlersuang, S. Stability of unsupported conical slopes in Hoek-Brown rock masses. *Transp. Infrastruct. Geotechnol.* **2021**, *8*, 278–295. [CrossRef]

48. Yodsomjai, W.; Keawsawasvong, S.; Lai, V.Q. Limit analysis solutions for bearing capacity of ring foundations on rocks using Hoek-Brown failure criterion. *Int. J. Geosynth. Ground Eng.* **2021**, *7*.
49. Shiau, J.; Al-Asadi, F. Revisiting circular tunnel stability using Broms and Bennermarks' Original Stability Number. *Int. J. Geomech.* **2021**, *21*, 06021009.
50. Shiau, J.; Chudal, B.; Mahalingasivam, K.; Keawsawasvong, S. Pipeline burst-related ground stability in blowout condition. *Transp. Geotech.* **2021**, *29*, 100587.
51. Shiau, J.; Keawsawasvong, S.; Lee, J. Three-Dimensional Stability Investigation of Trapdoors in Collapse and Blowout Conditions. *Int. J. Geomech.* **2022**, *22*, 04022007. [CrossRef]
52. Keawsawasvong, S.; Thongchom, C.; Likitlersuang, S. Bearing capacity of strip footing on Hoek-Brown rock mass subjected to eccentric and inclined loading. *Transp. Infrastruct. Geotechnol.* **2021**, *8*, 189–200. [CrossRef]
53. Keawsawasvong, S.; Yoonirundorn, K.; Senjuntichai, T. Pullout capacity factor for cylindrical suction caissons in anisotropic clays based on Anisotropic Undrained Shear failure criterion. *Transp. Infrastruct. Geotechnol.* **2021**, *8*, 629–644. [CrossRef]
54. Keawsawasvong, S.; Lai, V.Q. End bearing capacity factor for annular foundations embedded in clay considering the effect of the adhesion factor. *Int. J. Geosynth. Ground Eng.* **2021**, *7*.
55. Keawsawasvong, S.; Ukritchon, B. Undrained stability of a spherical cavity in cohesive soils using finite element limit analysis. *J. Rock Mech. Geotech. Eng.* **2019**, *11*, 1274–1285. [CrossRef]
56. Ukritchon, B.; Keawsawasvong, S. Design equations of uplift capacity of circular piles in sands. *Appl. Ocean. Res.* **2019**, *90*, 101844. [CrossRef]
57. Ukritchon, B.; Keawsawasvong, S. Unsafe error in conventional shape factor for shallow circular foundations in normally consolidated clays. *J. Geotech. Geoenvironmental Eng.* **2017**, *143*, 02817001. [CrossRef]
58. Ukritchon, B.; Keawsawasvong, S. Error in Ito and Matsui's limit equilibrium solution of lateral force on a row of stabilizing piles. *J. Geotech. Geoenvironmental Eng.* **2017**, *143*, 02817004. [CrossRef]
59. Sauer, T. *Numerical Analysis*, 3rd ed.; Pearson Education Ltd.: London, UK, 2014.